Monthly Notices
of the
ROYAL ASTRONOMICAL SOCIETY

MNRAS **495,** 4769–4781 (2020)
Advance Access publication 2020 May 23

doi:10.1093/mnras/staa1425

Detection of a variable ultrafast outflow in the narrow-line Seyfert 1 galaxy PG 1448+273

P. Kosec,[1]★ A. Zoghbi,[2] D. J. Walton,[1] C. Pinto,[3] A. C. Fabian,[1] M. L. Parker[4] and C. S. Reynolds[1]

[1]*Institute of Astronomy, Madingley Road, CB3 0HA Cambridge, UK*
[2]*Department of Astronomy, University of Michigan, Ann Arbor, MI 48109, USA*
[3]*INAF - IASF Palermo, Via U. La Malfa 153, I-90146 Palermo, Italy*
[4]*European Space Agency (ESA), European Space Astronomy Centre (ESAC), E-28691 Villanueva de la Cañada, Madrid, Spain*

Accepted 2020 May 19. Received 2020 May 19; in original form 2020 March 2

ABSTRACT

Relativistically blueshifted absorption features of highly ionized ions, the so-called ultrafast outflows (UFOs), have been detected in the X-ray spectra of a number of accreting supermassive black holes. If these features truly originate from accretion disc winds accelerated to more than 10 per cent of the speed of light, their energy budget is very significant and they can contribute to or even drive galaxy-scale feedback from active galactic nuclei (AGNs). However, the UFO spectral features are often weak due to high ionization of the outflowing material, and the inference of the wind physical properties can be complicated by other spectral features in AGNs such as relativistic reflection. Here we study a highly accreting narrow-line Seyfert 1 galaxy PG 1448+273. We apply an automated, systematic routine for detecting outflows in accreting systems and achieve an unambiguous detection of a UFO in this AGN. The UFO absorption is observed in both soft and hard X-ray bands with the *XMM–Newton* observatory. The velocity of the outflow is $(26\,900 \pm 600)$ km s^{-1} ($\sim 0.09c$), with an ionization parameter of $\log(\xi/\mathrm{erg\ cm\ s^{-1}}) = 4.03^{+0.10}_{-0.08}$ and a column density above 10^{23} cm^{-2}. At the same time, we detect weak warm absorption features in the spectrum of the object. Our systematic outflow search suggests the presence of further multiphase wind structure, but we cannot claim a significant detection considering the present data quality. The UFO is not detected in a second, shorter observation with *XMM–Newton*, indicating variability in time, observed also in other similar AGNs.

Key words: accretion, accretion discs – black hole physics – galaxies: Seyfert.

1 INTRODUCTION

Highly blueshifted absorption lines of ionized material have recently been detected in the X-ray spectra of a number of active galactic nuclei (AGNs), reaching velocities from $\sim 0.1c$ to as high as $0.5c$ (e.g. Pounds et al. 2003; Reeves, O'Brien & Ward 2003; Tombesi et al. 2010a, b, 2015; Nardini et al. 2015; Parker et al. 2017; Kosec et al. 2018c; Walton et al. 2019). These absorption lines could originate from accretion disc winds, launched at high velocities from the accretion flow of AGNs by radiation pressure (Proga, Stone & Kallman 2000) or magnetic forces (Fukumura et al. 2010). The large velocity and the consequent significant kinetic power make these outflows strong candidates for being the drivers of AGN feedback in galaxies (Fabian 2012; King & Pounds 2015). Alternatively, these blueshifted absorption lines could originate from low-density material co-rotating with the inner accretion flow without the need for an outflow from the system (Gallo & Fabian 2013; Fabian et al. 2020).

In most cases, the signatures of these so-called 'ultrafast outflows' (UFOs) were identified using the highly ionized features of Fe XXV and Fe XXVI (Tombesi et al. 2010a) in the iron *K* band (7–10 keV). The iron *K* band, however, is often on the upper edge of the energy range of the current instruments like *XMM–Newton* (EPIC pn and MOS) and *Chandra*, where the collecting area of the instruments steeply drops off, resulting in poor counts and signal-to-noise ratios. Additionally, this band commonly contains strong features of relativistically blurred reflection of the AGN coronal emission from the accretion disc (Tanaka et al. 1995; Fabian et al. 2009). Therefore, the observed absorption features can be hard to interpret as outflow signatures and it is difficult to infer the wind properties such as the velocity and the ionization level (Zoghbi et al. 2015). Furthermore, spurious low-significance features or lines of instrumental origin can be interpreted as real UFO signatures.

★ E-mail: pk394@cam.ac.uk

Less frequently, fast ionized wind absorption lines are also observed in softer X-rays (<5 keV), for example using the Si XIV, S XVI, and O VIII transitions (Jiang et al. 2018; Pinto et al. 2018; Reeves, Lobban & Pounds 2018a). The soft X-ray band (0.3–2.0 keV) can, however, be dominated by the commonly observed warm absorption from low-ionization material at larger distances from the AGN (e.g. Kaastra et al. 2000; Kaspi et al. 2002; Blustin et al. 2005; Detmers et al. 2011), which complicates line identification.

It is therefore important to study UFOs in different objects and across a broad X-ray band, comparing their properties to the source X-ray continuum properties in order to understand the true nature of UFOs and their relationship to AGNs.

Here we present the detection of a UFO with a velocity of 0.09c in the spectrum of a narrow-line Seyfert 1 galaxy PG 1448+273 observed with the *XMM–Newton* observatory. The signatures of the outflow are observed in both hard X-rays (iron *K* band) and soft X-rays (0.3–2.0 keV), and we constrain its physical properties systematically using an automated multiparameter search of the X-ray spectrum with photoionized absorption grids.

PG 1448+273 is a narrow-line Seyfert 1 AGN (Boller, Brandt & Fink 1996; Grupe et al. 2004) located at a redshift of $z = 0.0645$ (Alam et al. 2015). Its mass is $(9 \pm 2) \times 10^6\,M_\odot$ (Vestergaard & Peterson 2006, from single-epoch optical spectroscopy). PG 1448+273 has an estimated bolometric luminosity of $\sim 10^{45.5}$ erg s^{-1} (Grupe et al. 2004), resulting in an Eddington ratio above unity ($L/L_{\rm Edd} \sim 3$). PG 1448+273 could therefore be a super-Eddington accretor (Kawaguchi 2003). At such a high Eddington fraction, radiation pressure is an important component of the accretion flow and is expected to drive powerful outflows from the accretion disc (Shakura & Sunyaev 1973). PG 1448+273 is therefore a natural candidate for a spectroscopic search of UFO signatures.

Previous X-ray studies have remarked on the complex shape of the soft X-ray excess (Inoue, Terashima & Ho 2007) of PG 1448+273, requiring more than the usual ∼0.1 keV blackbody component for an accurate description. The AGN is, however, not heavily absorbed by neutral absorption or a strong warm absorber. Its X-ray spectrum is also highly variable (Ponti et al. 2012b).

This paper consists of five sections. The observation and data reduction are described in Section 2. Details of our analysis and the results are shown in Section 3, followed by a discussion of the findings in Section 5. Section 6 contains the conclusions of this study.

2 OBSERVATIONS AND DATA REDUCTION

The *XMM–Newton* (Jansen et al. 2001) data were obtained from the XSA[1] archive. The main data set consists of a single observation taken on 2017 January 24 (ID: 0781430101, proposal PI: A. Zoghbi) with a total raw exposure of 126 ks. There is also a second, much shorter (22 ks) observation, which was taken on 2003 February 8 (PI: Kawaguchi).

We reduced the main data set using standard pipelines with SAS v17. There were no high background periods of time during the observation and thus no time intervals needed to be filtered out.

The observation with the European Photon Imaging Camera (EPIC) pn and MOS instruments was split into two exposures, a scheduled ('S') part and an unscheduled ('U') part. Initially, we extracted the spectra of the two exposures separately, but found no significant differences between them. We therefore combined the scheduled and unscheduled parts of the observation into a single exposure.

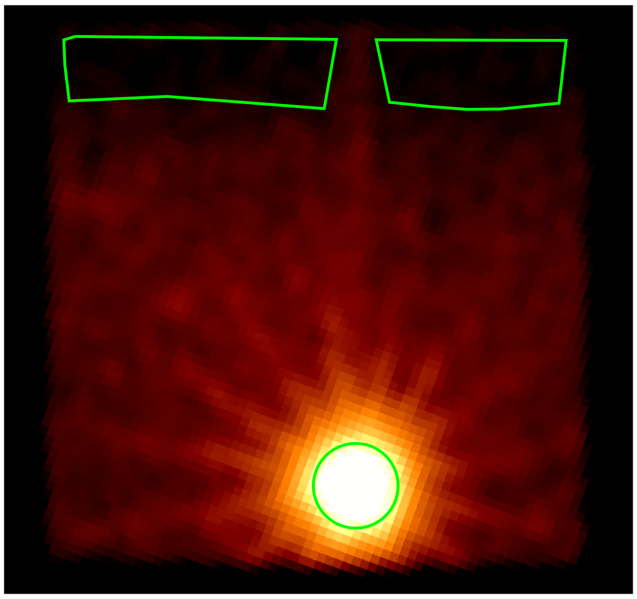

Figure 1. Image of the EPIC pn Small Window Mode exposure. The source region used in the analysis is the green circle (20 arcsec radius), and the two polygons are the regions used to extract the background spectrum. The non-uniform background count distribution (in the vertical direction) is evident and is likely caused by the wings of the source point spread function.

The EPIC pn (Strüder et al. 2001) instrument was operated in Small Window mode during the observation to limit pile-up. An image of the pointing was made using standard routines. We noticed a strong non-uniformity of background counts across the image (Fig. 1), likely due to source counts from the wing of the source point spread function (PSF). To avoid including source counts in the background spectrum, we chose background regions to be two small polygons as far from the source as possible. Furthermore, we decreased the importance of background subtraction by choosing a small (20 arcsec) source region. This boosted the signal-to-noise ratio in the critical 6–10 keV energy band where the Doppler-shifted absorption features of highly ionized iron (Fe XXV/XXVI) are expected. Only events of PATTERN <= 4 (single/double) were accepted. The average EPIC pn count rate was 2.2 ct s^{-1}, but the source is strongly variable, varying between 1 and 4 ct s^{-1} over the course of the observation.

EPIC/MOS 1 and 2 (Turner et al. 2001) were operated in Large Window mode. The source region was chosen to be a circle with a radius of 20 arcsec, similar to pn data. The background covered the rest of the central chip area, at least 110 arcsec away from the source, avoiding other bright point sources. We did not notice any background non-uniformity as observed in EPIC pn data, confirming that the non-uniformity observed in the EPIC pn image is caused by the wings of the PSF. Events of PATTERN <= 12 (single/double) were accepted. The average EPIC MOS 1 count rate was 0.44 ct s^{-1} and the average MOS 2 count rate was 0.43 ct s^{-1}. We stacked data from MOS 1 and MOS 2 into a single spectrum with the EPICSPECCOMBINE routine.

Data from both EPIC/pn and EPIC/MOS were grouped using the SPECGROUP procedure to at least 25 counts per bin, and to

[1] nxsa.esac.esa.int/nxsa-web/

oversample the detector resolution by a factor of at most 3. The clean exposure time of the pn data set is 76 ks, and the exposure of the combined MOS 1 and MOS 2 data is 108 ks (pn exposure is smaller due to a lower Live time in Small Window mode).

Reflection Grating Spectrometer (RGS; den Herder et al. 2001) data were reduced using standard routines with default values and with standard observational background. Data were binned by a factor of 3 directly within the SPEX fitting package to oversample the real grating resolution by roughly a factor of 3. The clean exposure of RGS 1 and RGS 2 data is 115 ks.

After reduction, the data were converted into SPEX FITS format using the TRAFO tool. SPEX fitting package (Kaastra, Mewe & Nieuwenhuijzen 1996) was used for spectral fitting as it contains the physically motivated ionized absorption grids XABS and PION. All spectral models were fitted using Cash statistics (Cash 1979) and the errors are stated at 1σ level. We use three cross-calibration constants to account for calibration differences between the four spectral data sets (pn, MOS, RGS1, and RGS2). The differences are smaller than 10 per cent in all cases.

EPIC pn and MOS data were initially ignored below 0.3 keV and above 10 keV following standard guidelines. RGS data were used in the range between 7.5 (1.7 keV) and 28 Å (0.44 keV), limited by strong background on both ends of this interval. We found a 10–15 per cent discrepancy between EPIC and RGS data in the 0.3–1.0 keV range that could be caused by poor spectral resolution of the EPIC instruments in this range or by calibration differences. At these energies, EPIC lacks the resolution to resolve the fine structure of absorption lines but would drive the spectral fits due to much higher count rates than RGS (resulting in much smaller errorbars compared to RGS data). To avoid confusion between different unresolved spectral components, we ignored EPIC pn and MOS data below 1.7 keV altogether in the main part of our analysis.

We followed the same steps to reduce and prepare the second observation (0152660101) for analysis. The statistics were naturally much worse compared to the main data set, albeit the AGN was brighter in 2003. The average EPIC pn count rate was 4 ct s^{-1}, and the average MOS 1/2 count rate was 0.9 ct s^{-1}. Since EPIC pn was operated in Large Window mode (with a pile-up limit of 3 ct s^{-1}), it is possible that the pn data are affected by pile-up. MOS was operated in Large Window mode (pile-up limit of 1.5 ct s^{-1}) and its data should not be affected. Nevertheless, we do not observe any significant differences between pn and MOS spectra. We ignored EPIC data below 1.7 keV, only using RGS data in the soft X-ray band, following the same procedure as with the main data set.

Fig. 2 contains the 1.7–10 keV EPIC pn spectra from both observations and shows the long-term variation of the source and the data set quality. Especially striking is the difference in the iron K region (5–8 keV). We first focus on the analysis of the higher quality observation (0781430101) that also shows more intriguing spectral features. The second observation is analysed separately in Section 4. It would not be appropriate to stack the two data sets given the long period of time and strong variability between the two observations.

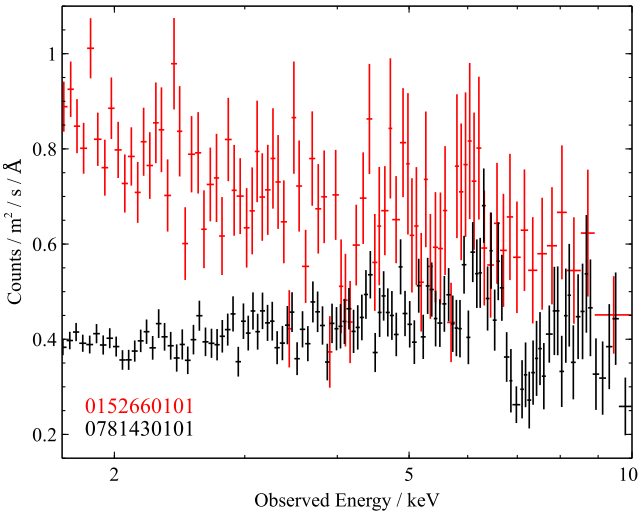

Figure 2. 1.7–10 keV EPIC pn spectra of PG 1448+273 during the two observations. Data from the main observation (0781430101) are in black colour, and data from the shorter archival observation (0152660101) are shown in red.

3 RESULTS FROM THE MAIN *XMM–NEWTON* OBSERVATION

3.1 Broad-band X-ray continuum

First we fit the broad-band 0.3–10 keV spectrum with a phenomenological X-ray AGN spectral model. We fit the RGS, EPIC pn, and MOS data simultaneously with the same spectral model except for the cross-calibration constant. The model consists of a power-law (POW in SPEX) model describing the inverse Compton coronal emission, a blackbody (BB) model describing the soft excess below 2 keV, and a relativistically blurred iron K emission line. Blurred reflection is described with a LAOR model applied to a Gaussian line (GA) with the energy fixed to 6.4 keV to avoid too much model freedom with the available data quality. All of these models are subject to any interstellar absorption in the host galaxy of the AGN described by a HOT model within SPEX. The model is then redshifted by $z = 0.0645$ of the host galaxy (found on the NED data base) using the REDS model. Finally, Galactic interstellar absorption is applied with a second HOT spectral model with a fixed value of $N_{\rm H} = 2.5 \times 10^{20}$ cm^{-2} (Kalberla et al. 2005). The final spectral model has the following form: HOT(REDS(HOT(POW+BB+LAOR×GA))).

We find that PG 1448+273 shows properties very similar to other narrow-line Seyfert 1 AGNs (for a summary of the continuum parameters, see Table A1). The power-law slope is measured to be 2.07 ± 0.03, and the soft excess can be described with a blackbody of temperature 0.097 ± 0.003 keV. The black hole appears to have a high spin value with a minimum disc radius of just $1.52^{+0.19}_{-0.29}$ $R_{\rm G}$, but we draw no firm conclusions since the relativistic iron K reflection is described only with a simple phenomenological model. The emissivity slope is $q = 4.6 \pm 0.5$ and the measured disc inclination is 44^{+2}_{-3} deg. We also find a significant non-zero interstellar absorption in the host galaxy of PG 1448+273 with a column density of $(9.8 \pm 2.1) \times 10^{20}$ cm^{-2}. The fit statistics are C-stat = 1594.43 for 1278 degrees of freedom.

Upon visual inspection of the spectrum, strong residuals in EPIC pn and MOS data within the iron *K* band are obviously evident (Fig. 3), as are residuals in the *RGS* band (Fig. 4). The iron *K*-band residuals suggest the presence of a highly ionized, high-velocity outflow; the flux drop above 7 keV is very similar to that of another NLS1 1H 0707−495 with a known high-velocity outflow (Boller et al. 2002; Kosec et al. 2018c). The RGS data point to a more complex situation. There is a prominent absorption residual at 18–19 Å (observed wavelength), which could correspond to O VIII absorption, blueshifted by $\sim 0.1c$. Further

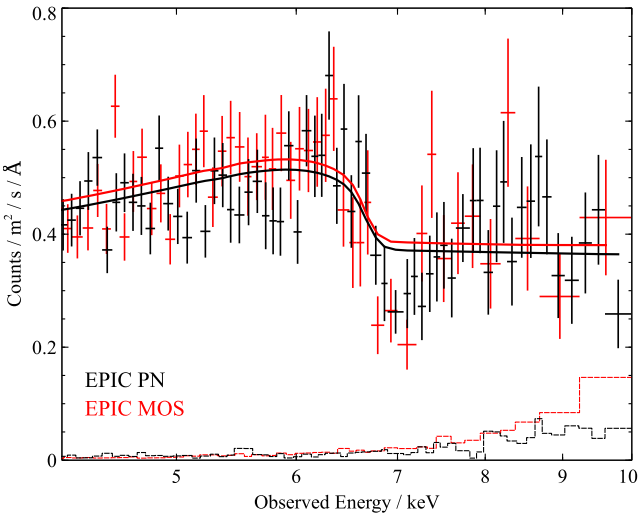

Figure 3. EPIC pn (black) and MOS (red, MOS 1 and MOS 2 stacked) data (4.5–10 keV) of PG 1448+273 fitted with the phenomenological AGN continuum model from Section 3.1. Apparent is the strong absorption residual observed at ∼7 keV. Black (pn) and red (MOS) solid lines show the best-fitting continuum models, and the dashed lines show the subtracted background spectra.

structures are also seen around 12 and 24 Å in observed wavelength.

3.2 Ionized wind search

3.2.1 Wind search set-up and results

To determine the blueshift and physical parameters of any ionized outflow component as well as its significance in the present data, we systematically scan the X-ray spectrum of PG 1448+273 with an automated ionized absorber search. In principle, we use a routine to scan a large parameter space of a photoionization absorber grid, to locate the best-fitting ionized outflow properties. Similar methods were recently successfully used to detect and study UFOs in ultraluminous X-ray sources (ULX; Kosec et al. 2018a, b; Pinto et al. 2020).

The photoionization model we use here to describe the spectral features (absorption lines) of an ionized outflow is called XABS in the SPEX fitting package. The model calculates the ionizing balance and absorption line strengths based on the spectral energy distribution (SED) shape of the AGN NGC 5548 (Steenbrugge et al. 2003, 2005). The SED of NGC 5548 should be a reasonable approximation for the PG 1448+273 SED, although the former is likely more massive at $(9 \pm 3) \times 10^7$ $M_\odot$, and has a smaller Eddington ratio (Lu et al. 2016). The coronal power-law slope of NGC 5548 is $\Gamma \approx 1.8$ versus $\Gamma = 2.07 \pm 0.03$ in PG 1448+273, so PG 1448+273 has a softer spectrum but not as soft as the more extreme NLS1 AGNs like IRAS 13224−3809 where Γ varies between 2.2 and 2.9 (Pinto et al. 2018). At each step, we also check our results for consistency with the PION model in the SPEX fitting package. PION is a similar model of photoionized plasma as XABS but it takes into account the actual continuum SED of the currently used spectral model, albeit at a much higher computational cost, which is the limiting factor in our analysis.

The main parameters of the XABS model are the column density $N_{\rm H}$, ionization parameter $\log \xi$, systematic velocity z, and turbulent velocity (or simply velocity broadening) $v_{\rm turb}$ of the ionized absorber. An outflow in the X-ray spectrum of the AGN can in principle have any blueshift, ionization parameter, column density, and turbulent velocity. This is a large parameter range that has to be searched in an automated way to avoid missing the parameter space with the best-fitting solution. As an added bonus, performing a systematic search in this way will allow us to constrain the statistical significance of any outflow detection in the AGN spectrum.

We therefore create a grid of photoionization models that spans ionization parameters between $\log(\xi/{\rm erg\ cm\ s^{-1}}) = -1.0$ and 4.8 with a grid spacing of $\Delta \log \xi = 0.2$ (in line with the recommendation of Reynolds et al. 2012), with three fixed turbulent velocities of $v_{\rm turb} = 100$, 1000, and 10 000 km s^{-1}. The turbulent velocity space grid is chosen to be coarse to decrease the computational cost of the automated search.

Afterwards a range of realistic systematic absorber velocities (blueshifts) is chosen. We choose to search for an absorber with a systematic velocity between +20 000 km s^{-1} (to account for possible infalling gas) and −100 000 km s^{-1} (blueshift of roughly 0.4c, after relativistic correction). The step size is 150 km s^{-1} for turbulent broadening of 100 and 300 km s^{-1} for turbulent broadening of 1000 km s^{-1}. This is chosen so that in each case the step size is not much larger than the broadening and at the same time is not much larger than the spectral resolution of our detectors, RGS being the best of our instruments with a spectral resolution of roughly ∼300 km s^{-1} in velocity units. In the case of turbulent velocity equal to 10 000 km s^{-1}, the features are so broad that such detailed sampling is not necessary, instead we sample by 1000 km s^{-1}.

We generate an absorption grid for every possible systematic velocity, ionization parameter, and broadening within the selected range, add this model to the baseline continuum from Section 3.1, and fit for the column density of the absorber (with the remaining absorber parameters fixed), leaving the continuum parameters free to vary. If an absorber of such parameters is disfavoured by the data, the resulting column density will be 0, i.e. the best-fitting solution is the null (baseline continuum) model. Otherwise, we recover the best-fitting absorber column density as well as the ΔC-stat fit improvement obtained by adding the photoionization grid to the (null) baseline continuum model. Any improvement in the ΔC-stat fit statistics compared to the null model is recorded for every point in the multidimensional search grid, and determines how strongly the spectral model including the wind absorption is preferred to the baseline continuum model.

We search the large parameter space for signatures of an ionized outflow as described above, using the full data set (RGS + pn + MOS) on PG 1448+273. The results of the search are shown in Fig. 5. The wind search achieves a strong detection of ionized plasma with a systematic outflow velocity of ∼30 000 km s^{-1}, with a fit improvement of ΔC-stat > 70. The plasma is highly ionized with $\log \xi$ of 4.0–4.2 and the fit improvement is much higher in the scans with a 1000 or 10 000 km s^{-1} turbulent velocity compared to the one with 100 km s^{-1} velocity width. All the other ΔC-stat peaks in the systematic scans are much smaller, reaching at most ΔC-stat ∼30–35; hence, the 'primary' (strongest) solution is highly preferred.

The fact that our detection is above ΔC-stat = 70 already strongly suggests the significance of this outflow component, comparing with previous similar analyses (e.g. Kosec et al. 2018b). However, due to the look-elsewhere effect, since we are searching through a large parameter space, it is not trivial to assign directly a 'wind detection significance' to a specific value of ΔC-stat (Protassov et al. 2002). Monte Carlo simulations must be employed to rigorously 'map' the

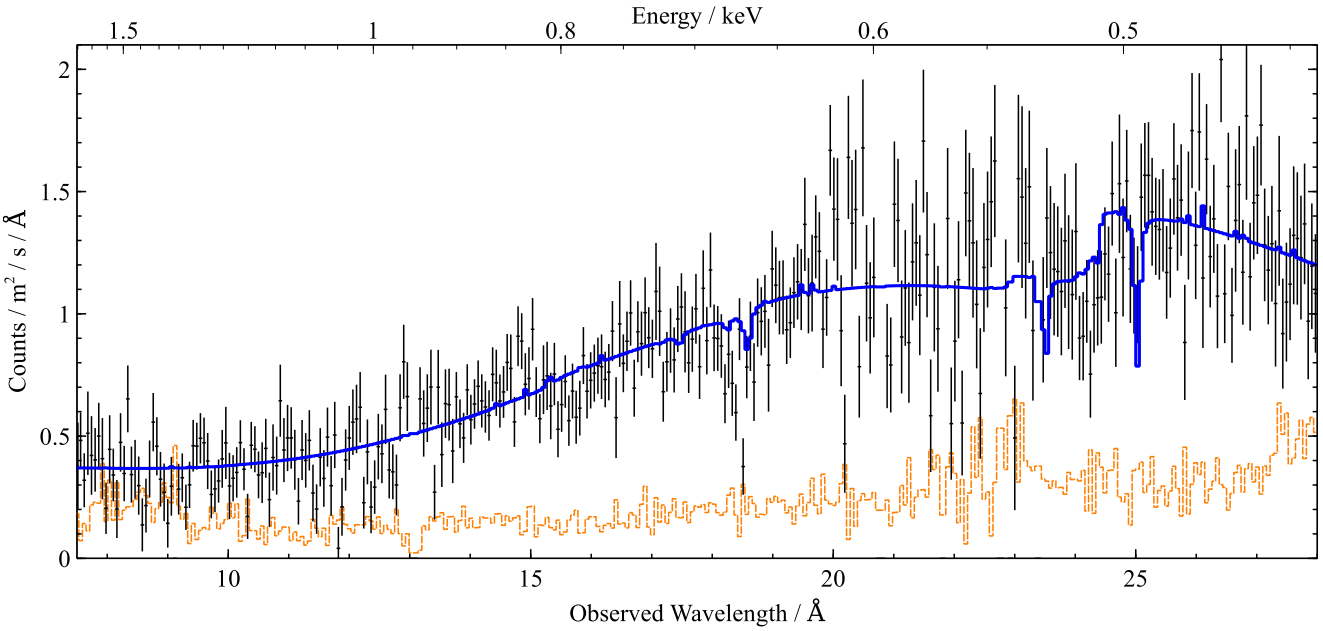

Figure 4. Background-subtracted RGS data (7.5–28 Å) of PG 1448+273, stacked and overbinned for plotting purposes only, fitted with the phenomenological AGN continuum model from Section 3.1 (blue colour). The model particularly fails to reproduce the strong residuals around 18–19 Å; however, further residuals are seen around 12, 15.5, and 24 Å. The edge at 24.5 Å and the strong absorption line at 25 Å suggest the presence of neutral absorption intrinsic to the AGN. The subtracted background is shown in orange.

C-stat fit improvement to a specific false alarm probability for each wind detection. The results of Monte Carlo simulations are shown in Appendix B. They indicate that the significance of the primary peak detection is well above 3σ–4σ and thus our UFO detection is robust.

3.2.2 Secondary detections in the wind search

We also find a large number of secondary peaks with ΔC-stat between 25 and 35 which by themselves could be considered significant detections, if they were detected alone. Their presence suggests that there could be further wind structure hiding in the spectrum of PG 1448+273. However, at this point it is not certain that the secondary peaks are independent of the primary peak. These secondary solutions could in fact be fitting some of the same spectral residuals to the baseline continuum as the primary peak, but with a different set of atomic lines, resulting in a shallower ΔC-stat improvement.

Finally, we also notice a ΔC-stat peak around the rest frame of the AGN in the 100 km s^{-1} velocity width search. The peak is not particularly strong with ΔC-stat ∼ 20 at the ionization parameter of $\log(\xi/\mathrm{erg\ cm\ s^{-1}}) = -0.6$, but it could mean the presence of a weak warm absorber. Absorbers with similar ionization parameters are very commonly observed in other AGNs (e.g. Blustin et al. 2005); it is thus not unlikely that one could also appear in the spectrum of PG 1448+273. If this is the case, the same look-elsewhere effect as for the UFO detection does not apply. Warm absorbers in particular only appear over a very small systematic velocity parameter space (velocities from hundreds of km s^{-1} to a few thousands of km s^{-1} at maximum). The same ΔC-stat significance rules for UFO detections hence do not apply as the available parameter space is much smaller, and a significantly weaker warm absorber detection might still represent real absorption features. For this reason, we fit both the features of the UFO primary peak as well those of the warm absorber in the next section.

3.3 UFO and warm absorption

To learn more about the properties of the ionized absorbers in PG 1448+273, we fit its spectrum directly with a model that includes the original baseline continuum (with all the parameters freed), plus two ionized absorbers described with the XABS model. The first XABS model is supposed to fit the primary peak in the systematic absorber search at around 30 000 km s^{-1}, and the second one should fit the possible features of a warm absorber in the rest frame of the AGN.

The primary ultrafast component is found with an outflow velocity of 26 900 ± 600 km s^{-1} (including the relativistic correction). Its column density is $0.28^{+0.12}_{-0.07} \times 10^{24}$ cm^{-2}, with an ionization parameter of $\log(\xi/\mathrm{erg\ cm\ s^{-1}}) = 4.03^{+0.10}_{-0.08}$ and a velocity width of 2100^{+600}_{-500} km s^{-1}. The final fit improvement of adding this component to the baseline model is very strong with ΔC-stat = 83.27, confirming the significance of the UFO features in the spectrum of PG 1448+273. The strongest spectral features of the UFO absorption are the Fe XXV and Fe XXVI lines at ∼7 keV (in the EPIC band) and the O VIII line at 18.5 Å (∼0.7 keV, in the *RGS* band).

The warm absorber has a column density of $(3.8 \pm 1.7) \times 10^{20}$ cm^{-2} and an ionization parameter of $\log(\xi/\mathrm{erg\ cm\ s^{-1}}) = -0.4^{+0.3}_{-0.4}$. Its systematic velocity is -100 ± 200 km s^{-1} in the rest frame of the AGN, so it is consistent with being at rest, with a velocity width of 50^{+40}_{-30} km s^{-1}. It is similar to warm absorbers found in other AGNs (Kaspi et al. 2002; Steenbrugge et al. 2005; Detmers et al. 2011), apart from the column density that is much lower in PG 1448+273, resulting in rather weak spectral features, and a lower ΔC-stat fit improvement of 15.19. The ΔC-stat is smaller than the original value found in the automated wind search (∼20), suggesting that

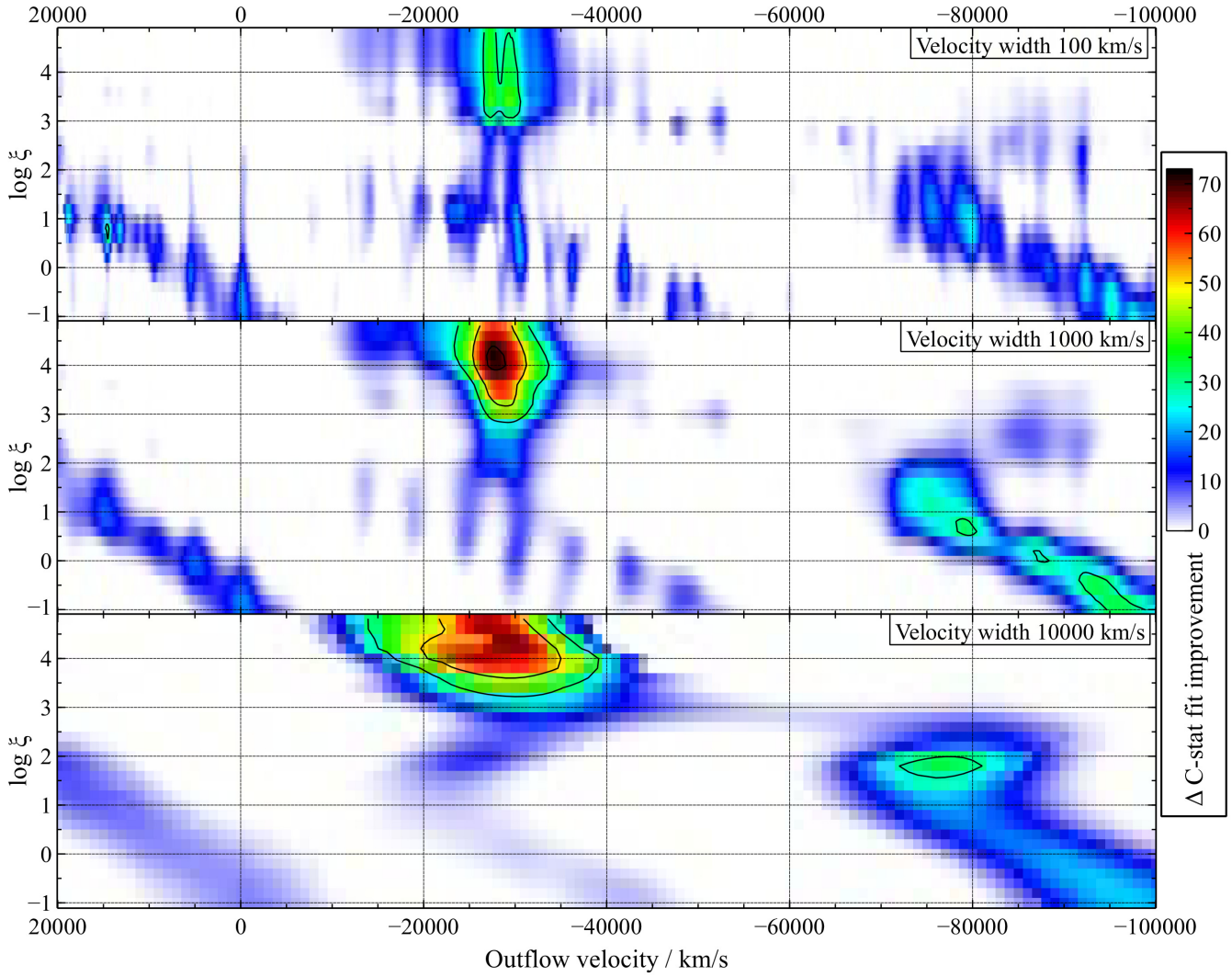

Figure 5. Systematic scan for ionized outflow features in the spectrum of PG 1448+273. The spectrum is scanned with ionized absorption model grids with systematic velocities between +20 000 and −100 000 km s^{-1} (on the *X*-axis), ionization parameters log ξ between −1.0 and +4.8 (on the *Y*-axis), with turbulent velocities of 100 km s^{-1} (top subplot), 1000 km s^{-1} (middle subplot), and 10 000 km s^{-1} (bottom subplot). The colour shows the ΔC-stat fit improvement upon adding the absorption grid to the baseline continuum model (according to the colour bar on the right), and the black contours show ΔC-stat fit improvement of 30, 50, and 70, respectively.

the ultrafast and warm absorber models are partly fitting the same residuals to the original baseline continuum. The spectral features of the warm absorber are located at around 24 Å in the *RGS* band.

Since the strongest absorption lines of the warm absorption lie in the 24 Å range, they overlap with the N VII absorption of the 0.1*c* ultrafast phase. It is therefore possible that these features instead could originate in N VII absorption of the ultrafast phase. We attempt to describe the features by freeing the abundance of N in our final spectral model (with the warm absorber column density fixed to 0), and reach fit statistic improvements at a ΔC-stat ≈10 level (compared to a continuum + UFO with solar abundances spectral model), for a nitrogen overabundance of 7^{+3}_{-2}. We consider this to be a very high abundance value and prefer the warm absorption origin for the 24 Å features as a far more likely explanation.

The baseline continuum parameters slightly shift (for a summary of the continuum parameters, see Table A1), with the best-fitting power-law slope being 1.97 ± 0.03 and the soft excess blackbody temperature of 0.102 ± 0.003 keV; however, they still agree with the original continuum fit values within ∼3σ errors. The inner disc radius (from the iron K line) is 1.7 ± 0.5 R_G, the emissivity slope is $3.5^{+2.1}_{-0.5}$ and the disc inclination is found to be 38^{+16}_{-3} deg. Most notably, the best-fitting neutral absorber (in the rest frame of PG 1448+273) is now weaker with a column density of $6.5^{+2.0}_{-2.2} \times 10^{20}$ cm^{-2}. This could be explained if the warm absorber (with a low ionization parameter) is fitting similar spectral residuals as the neutral absorption. The final fit statistics are C-stat = 1495.97 for 1270 degrees of freedom.

The best-fitting wind spectral model is shown in Fig. 6 (EPIC pn and MOS data only) and in Fig. 7 (RGS data only).

3.4 Residual structure in the X-ray spectrum – a multiphase outflow?

The large C-stat value of the best-fitting spectral model given the number of degrees of freedom, and the secondary peaks in the systematic wind search suggest the presence of further ionized

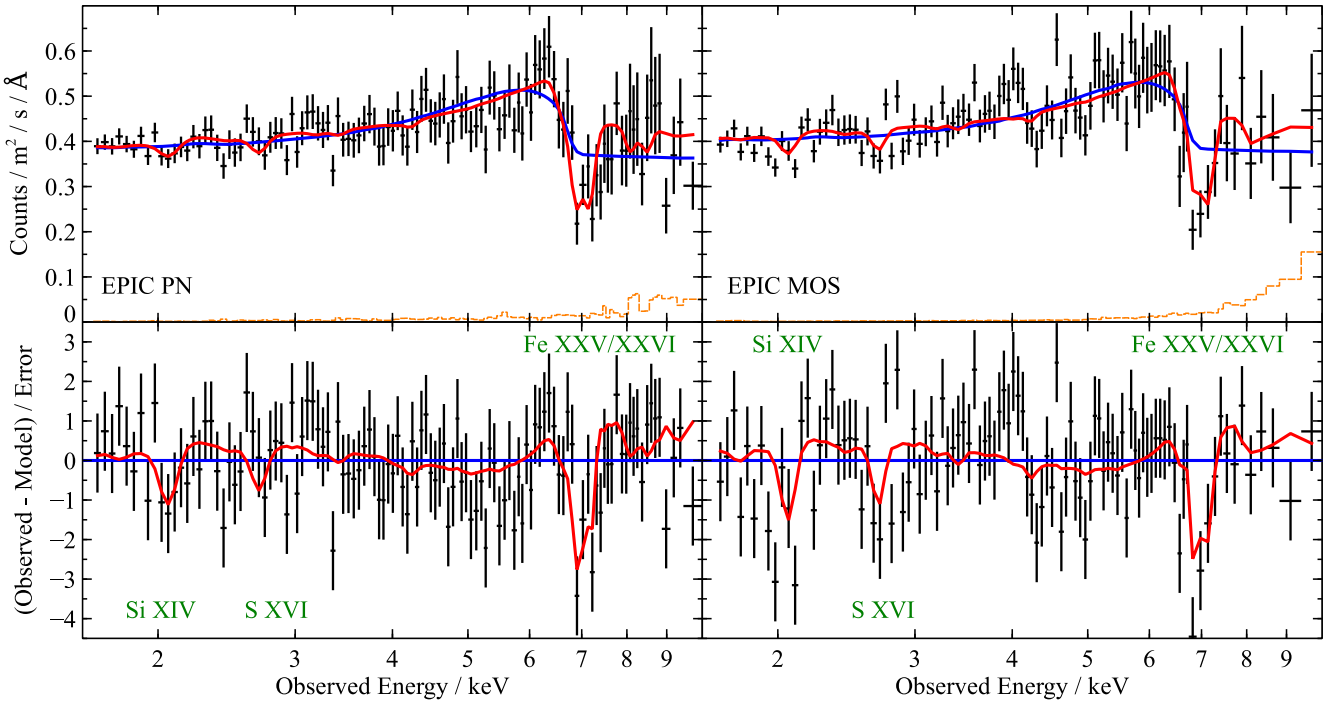

Figure 6. EPIC pn (left subplots) and MOS (right subplots) data (1.7–10 keV) of PG 1448+273 fitted with the phenomenological AGN continuum model from Section 3.1, plus two wind components: one ultrafast, highly ionized component outflowing at ∼27 000 km s^{-1}, and a warm absorber component in the rest frame of the AGN. The top subplots show the spectra with the best-fitting baseline continuum (blue colour) and the continuum + wind models (red colour), and the bottom subplots contain the residuals to the continuum model as well as the best-fitting wind solution (red). The orange dashed lines show the subtracted background spectra. Green labels name the strongest absorption lines of the UFO absorption.

outflow components in the spectrum of PG 1448+273, assuming that our baseline continuum model is accurate. However, the secondary peaks might not be independent of the primary wind detection, i.e. their spectral signatures could be shared. For this reason, it does not make sense to directly fit the secondary peaks based on the existing automated wind search (Fig. 5).

We therefore perform a new set of wind searches that includes the two outflow components described above (in Section 3.3). We choose the best-fitting baseline continuum with two additional XABS components (UFO and warm absorber) to be the new baseline model. We then run the same wind search as described in Section 3.2, with all the baseline continuum parameters allowed to vary freely. The results are shown in Fig. 8.

There are no strong wind detections in the search with a turbulent velocity of 1000 km s^{-1}. On the other hand, there are roughly five peaks with fit improvements between ΔC-stat of 15 and 22 in the search with 100 km s^{-1} turbulent velocity, suggesting tentative evidence of further ionized outflow components. Furthermore, there is a similarly strong peak (ΔC-stat ∼ 20) in the 10 000 km s^{-1} width search.

If only a single peak with a similar fit improvement (ΔC-stat ∼ 20) was detected, it would be trivial to assign a false alarm probability to its detection based on our Monte Carlo simulation results from Appendix B. However, the fact that there are six peaks with similar ΔC-stat values means that we likely cannot statistically differentiate which of these solutions are real and which are false detections as they will all result in similar statistical significances/false alarm probabilities. The situation is further complicated because these peaks are probably not independent, i.e. multiple potential peaks are fitting the same residuals to the baseline continuum, but with different outflow models.

We individually fit each of the peaks with ΔC-stat >15 but find no further fit improvement or any particularly strong outliers. The tentative solutions mostly fit residuals in the RGS band, in particular those at 12–13 Å, at 15–16 Å, and in the 20–22 Å range (Fig. 7). At the current data quality, these residuals can be fitted equally well with multiple wind models. Since multiple wind solutions fit the RGS residuals similarly well, we cannot identify a unique solution with the present data. We find that none of the tentative peaks fit the remaining residuals seen in the iron *K* band, which could instead be interpreted as our imperfect fitting of the relativistic reflection with just the phenomenological LAOR model (omitting the reflection continuum).

The large abundance of peaks with ΔC-stat of around 15–20, however, still suggests a very likely presence of a multiphase outflow in PG 1448+273 because such strong false detections should occur rarely by chance. Based on our MC simulations, even accounting for their limited parameter space, we can very roughly assign a 2σ statistical significance (including the look-elsewhere effect) to a ΔC-stat = 16 outflow detection. Such strong fake detections should therefore only occur in 5 per cent of observations, suggesting that the secondary peaks are real. At this moment, unfortunately, identification of these potential components is just beyond the possibilities of the current data quality.

4 ARCHIVAL SHORT *XMM–NEWTON* OBSERVATION

We apply the same continuum model as used in Section 3.1 to the second, archival data set. Due to lower data quality, we fix the blurred iron K line parameters to the best-fitting parameters from the final fit in Section 3.3, which included the broad-band continuum as

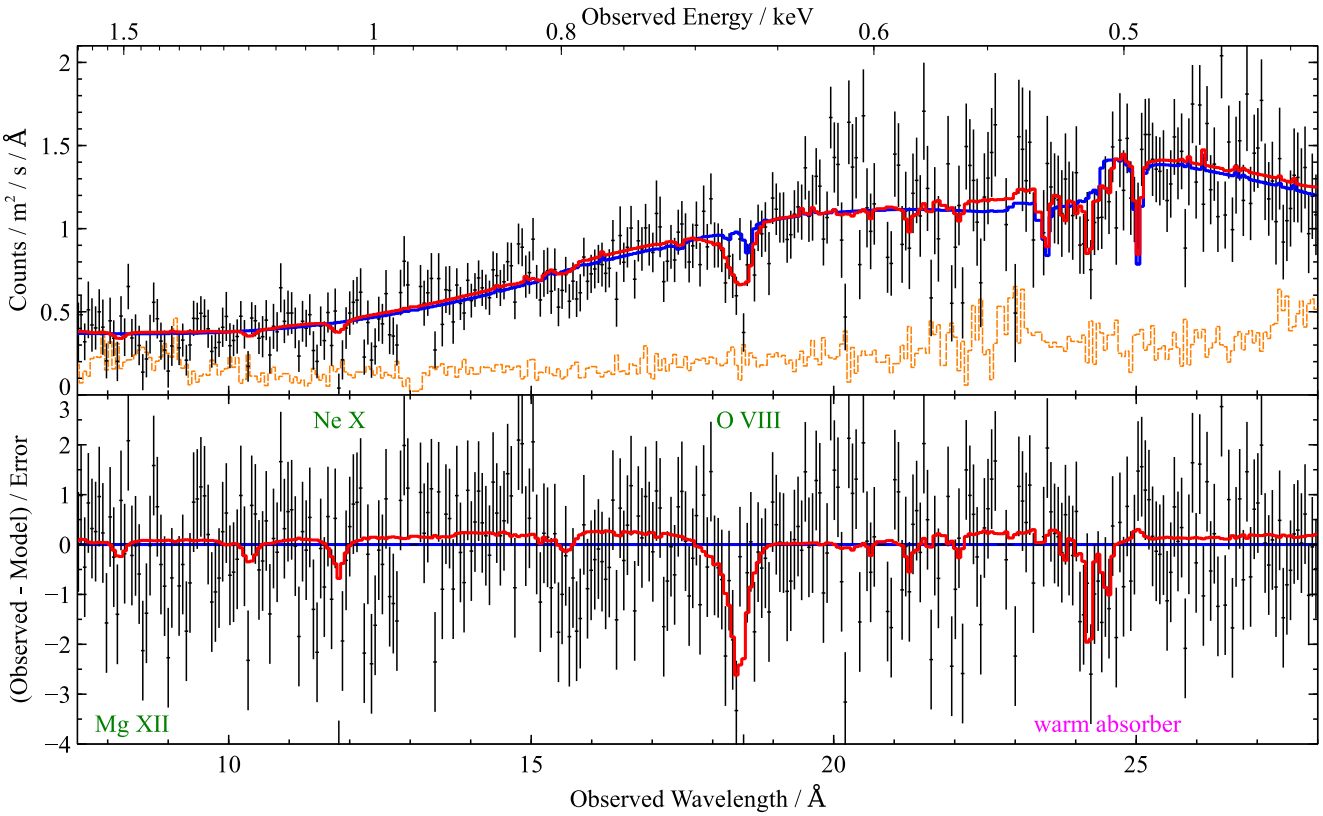

Figure 7. RGS data between 7.5 Å (1.7 keV) and 28 Å (0.4 keV) of PG 1448+273, stacked and overbinned for plotting purposes only, fitted with the phenomenological AGN continuum model from Section 3.1, plus two ionized components: one ultrafast, highly ionized component moving at ∼27 000 km s^{-1}, and a warm absorber component in the rest frame of the AGN. The top subplot contains the RGS spectrum fitted with the baseline continuum (blue colour) and continuum + wind (red colour) models, and the bottom subplot shows the residuals to the continuum model and the best-fitting wind solution (red). The subtracted background in orange colour. Green labels name the most notable absorption lines of the UFO absorption and the magenta label shows the spectral features of the warm absorber.

well as the ultrafast and warm absorption. We find that the coronal power-law slope is much higher with $\Gamma = 2.38 \pm 0.04$, and the average 2–10 keV luminosity is $(2.16 \pm 0.07) \times 10^{43}$ erg s^{-1}.

Since the statistics are much worse, the addition of neutral absorption intrinsic to the AGN is not significant. The best-fitting spectrum is shown in Fig. 9 (EPIC data) and Fig. 10 (RGS data). The data are of lower quality than from the other observation, but we do not notice any strong absorption features at 7 keV or at 18 Å as seen in the previous data set, or any other absorption signature of a UFO. Interestingly, it appears that an emission feature is present at 18 Å instead (Fig. 10). If the feature is real, it could be due to Fe XVII emission (rest-frame wavelength 17.1 Å) or blueshifted O VIII emission (rest-frame wavelength 19.0 Å).

As a further check, we add the same UFO absorption as observed in the long exposure data set to the baseline continuum of the short observation. We use the best-fitting UFO parameters from Section 3.3. The resulting spectral model is shown in Figs 9 and 10 (red colour), and is clearly rejected by the data. The 1σ upper limit on the column density of such absorber is just 1.7×10^{22} cm^{-2}, more than 10 times lower than the column density observed in the other *XMM–Newton* observation. We cannot exclude a possibility that a UFO of the same column density is present, but with a higher ionization parameter. However, the change in the ionization parameter would have to be significant, with a lower limit on the ionization parameter of about $\log(\xi/\mathrm{erg\ cm\ s^{-1}}) \approx 5$. Such a large change in the ionization parameter (10× higher) would require a non-linear response between the absorber and the ionizing luminosity of PG 1448+273.

Finally, we apply the same systematic wind search from Section 3.2 to locate any potential absorption with parameters different to that of the UFO observed in the other observation. As the data quality is much lower compared to the first exposure and there are no strong spectral residuals, we do not find any significant detections (ΔC-stat >15).

5 DISCUSSION

We have performed a systematic search for an ionized outflow in the X-ray spectrum of the narrow-line Seyfert 1 AGN PG 1448+273. We significantly detect a highly ionized wind with a velocity of $(0.090 \pm 0.002)c$.

The absorption lines of the outflow are detected in both hard X-rays (iron *K* band) and soft X-rays (0.3–2.0 keV, particularly the O VIII line). This suggests that the wind is not as extremely ionized as in other AGNs and X-ray binaries where often only Fe XXV/XXVI features are observed (e.g. Tombesi et al. 2010a; Ponti et al. 2012a). This fact simplifies the inference of the wind parameters as it reduces the uncertainties in both the velocity and ionization state of the outflow while simultaneously modelling the wind features as well as the iron K reflection.

The velocity of the outflow of ∼0.1*c* is also not as high as seen in many other AGNs (for a review of the recent UFO detections

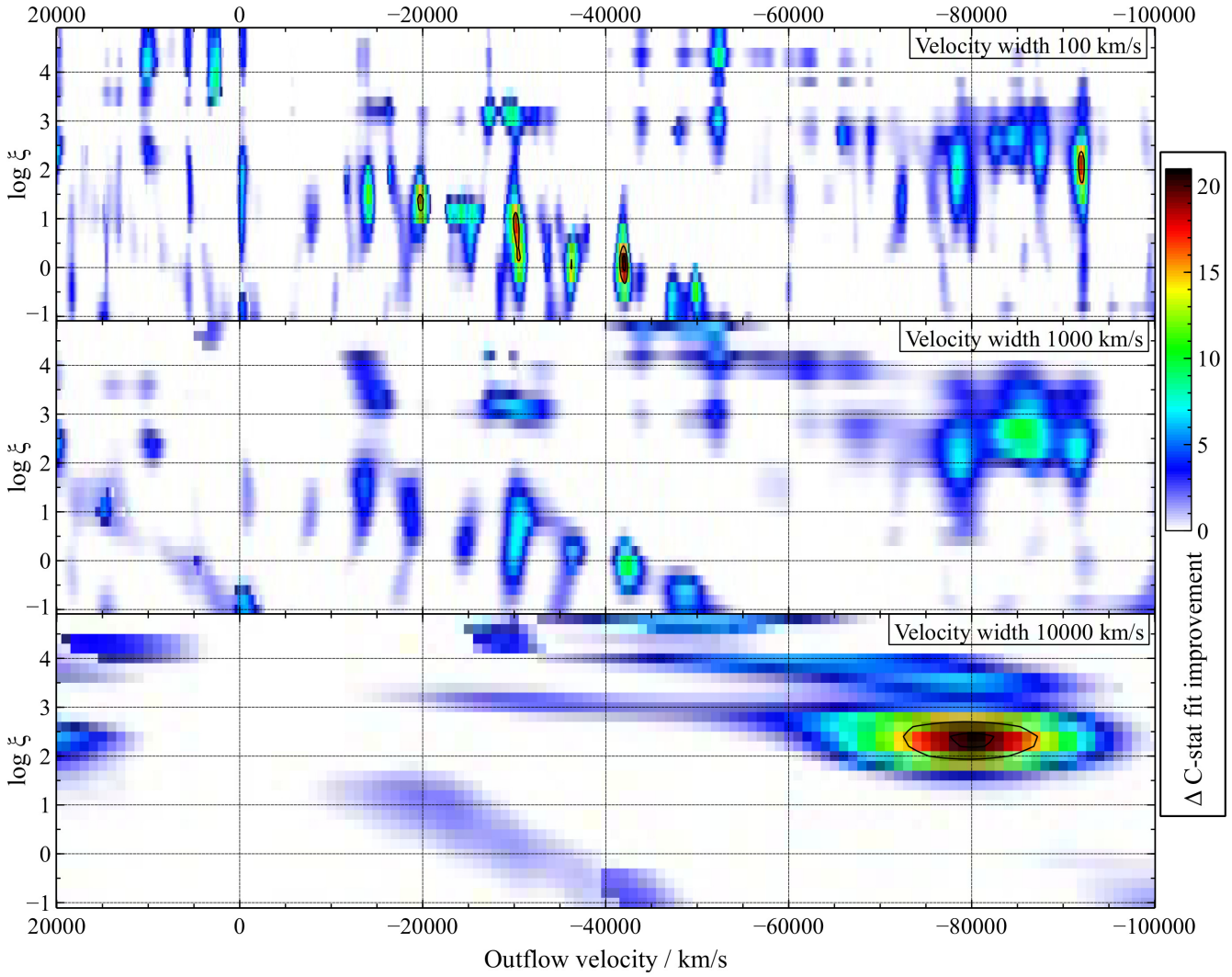

Figure 8. Systematic scan for ionized outflow features in the spectrum of PG 1448+273, in addition to the primary ultrafast component outflowing at 27 000 km s^{-1} and a warm absorber component in the AGN rest frame. The spectrum is scanned with ionized absorption grids with systematic velocities between +20 000 and −100 000 km s^{-1} (the *X*-axis), ionization parameters log ξ between −1.0 and +4.8 (the *Y*-axis), with a turbulent velocity of 100 km s^{-1} (top subplot), 1000 km s^{-1} (middle subplot), and 10 000 km s^{-1} (bottom subplot). The colour shows the fit improvement ΔC-stat upon adding the absorption grid to the continuum model (according to the colour bar on the right), and the black contours show ΔC-stat fit improvement of 15 and 20, respectively.

and their velocities, see Parker et al. 2018a), where velocities as high as 0.3*c*–0.5*c* were detected (e.g. Reeves et al. 2018b; Walton et al. 2019, are the most extreme examples), although velocities in the range of 0.05–0.1*c* have also been detected in some AGNs (e.g. Pounds et al. 2016a). Similarly, the velocity width of the observed features is not large at 2100^{+600}_{-500} km s^{-1}. This suggests that the AGN corona ionizing the atoms within the outflow cannot be either too large or too close to where the wind absorption occurs as otherwise the toroidal motion within the wind (imprinted to the wind by the Keplerian rotation of the accretion disc) would broaden the absorption features (Fukumura & Tombesi 2019).

We also note that the outflow velocity is lower than that of the UFO observed in IRAS 13224−3809 (0.25*c*; Parker et al. 2017). At the same time, the inclination of PG 1448+273 (∼40°) is lower than the inclination of IRAS 13224−3809 (about 70°; Jiang et al. 2018). A lower UFO velocity in PG 1448+273 would be expected in the framework of a model where the UFO absorption is produced in an atmosphere co-rotating with the accretion disc (Fabian et al. 2020) because the projected disc velocities are lower in PG 1448+273.

Curiously, the UFO is not detected in the short (20 ks) 2003 *XMM–Newton* observation of PG 1448+273 (Appendix 4). The data set is good enough to significantly reject a UFO of parameters similar to that observed in the main data set. It is possible that the UFO is still present but at much higher ionization or with a much lower column density. A change in the outflow velocity alone cannot explain the disappearance of absorption lines from both EPIC and particularly RGS data. Interestingly, PG 1448+273 shows a higher flux during the shorter observation when the UFO is not seen. This is a similar behaviour to that of IRAS 13224−3809, which hosts a time-variable UFO, which anticorrelates in absorption strength with the AGN X-ray flux (Parker et al. 2017; Pinto et al. 2018). Further long exposures with *XMM–Newton* will be required for a proper flux-resolved analysis to confirm the existence of this important trend in PG 1448+273.

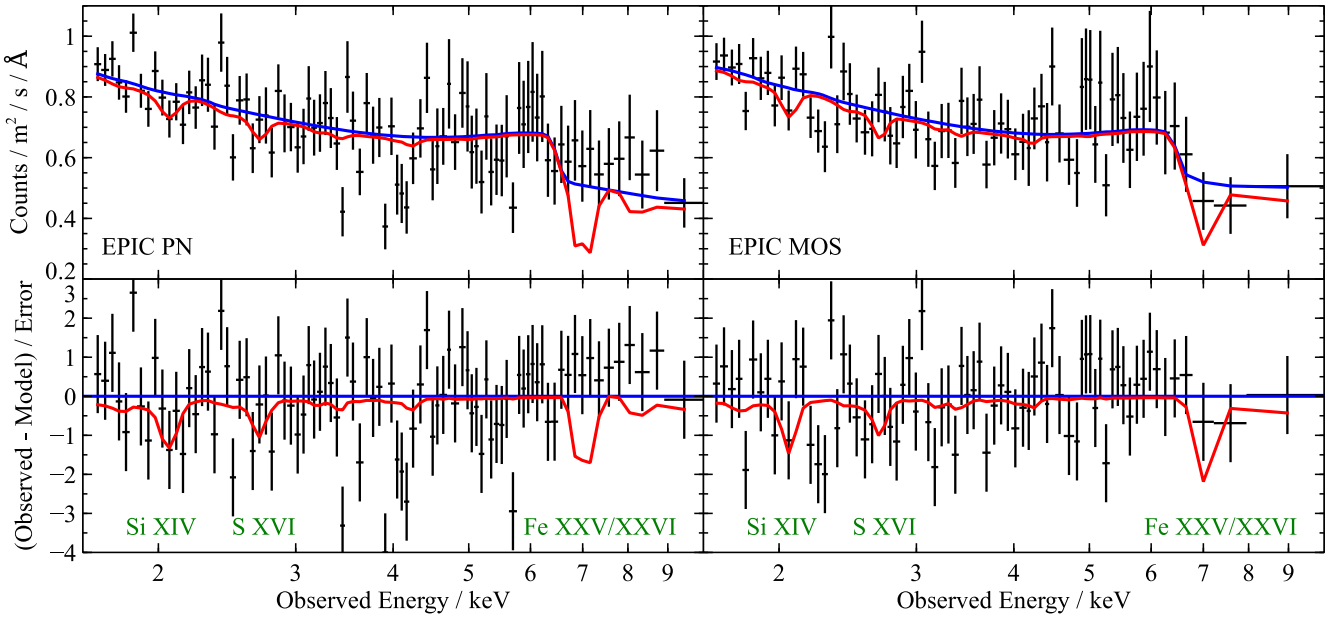

Figure 9. EPIC pn (left subplots) and MOS (right subplots) data (1.7–10 keV) of the second, short observation of PG 1448+273 fitted with the baseline continuum model from Appendix 4 (blue colour). The model in red colour is the best-fitting baseline continuum plus one UFO component with the parameters of the outflow detected in the long *XMM–Newton* observation (Section 3.3). The top subplots show the fitted spectra, and the bottom subplots contain the residuals. Green labels name the strongest absorption lines of the UFO absorption.

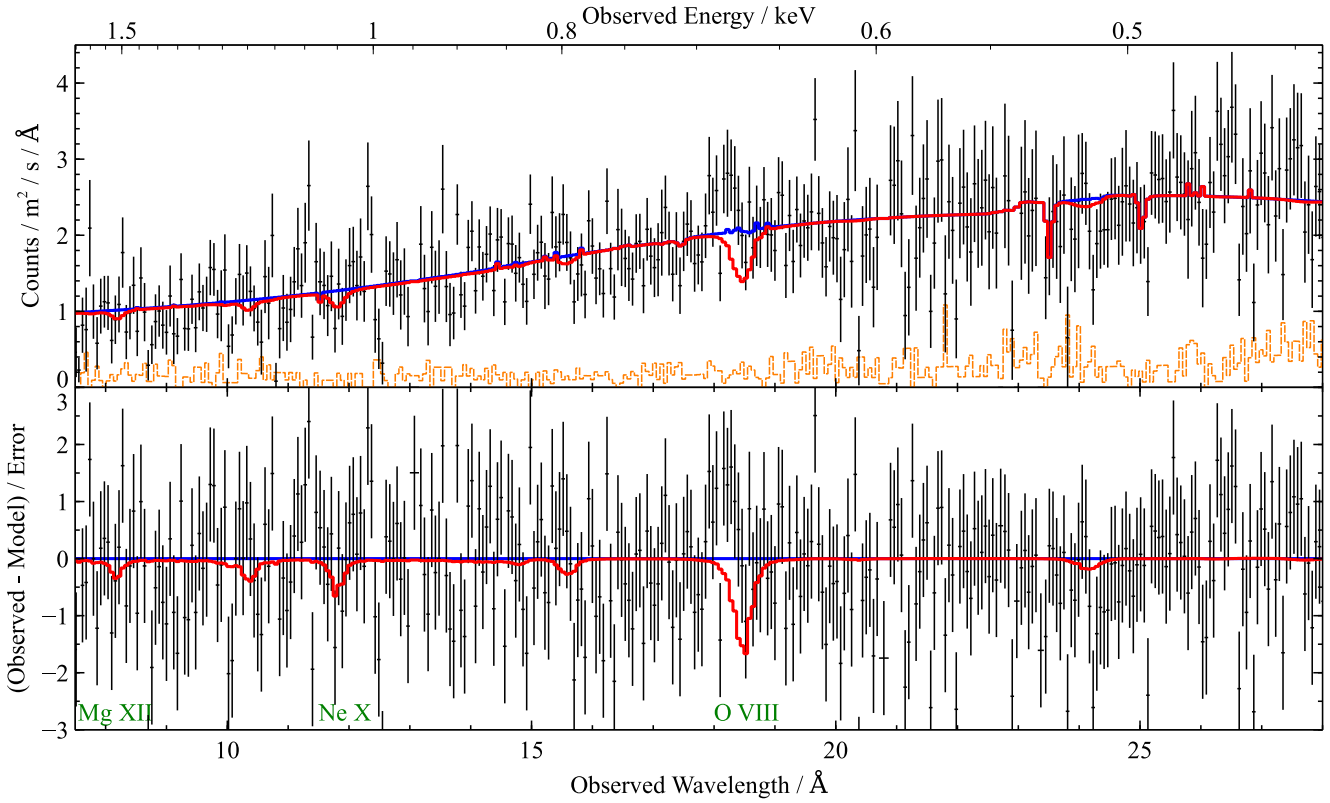

Figure 10. RGS data between 7.5 Å (1.7 keV) and 28 Å (0.4 keV) of the second, short observation of PG 1448+273, stacked and overbinned for plotting purposes only, fitted with the baseline continuum model from Appendix 4 (blue colour). The model in red colour is the best-fitting baseline continuum plus one UFO component with the parameters of the outflow detected in the long *XMM–Newton* observation (Section 3.3). The top subplot shows the fitted spectra, and the bottom subplot contains the residuals. Green labels name the strongest absorption lines of the UFO absorption.

We also detect a weak warm absorber in PG 1448+273. Warm absorbers were detected in multiple AGNs with UFO detections, including PG 1211+143 (Reeves et al. 2018a), PG 1114+445 (Serafinelli et al. 2019), IRAS 17020+4544 (Leighly et al. 1997; Longinotti et al. 2015), and IRAS 13349+2438 (Sako et al. 2001; Parker et al. 2018b). Comparing their energetics and mass outflow rates can be helpful in explaining their (possibly common) origin (Tombesi et al. 2013) and their interaction with the surrounding environment. Unfortunately, the warm absorber in PG 1448+273 has a very small outflow velocity of 100 ± 200 km s^{-1}, consistent with being at rest. The limits placed on its energetics are therefore not useful.

We search the X-ray spectrum of PG 1448+273 for further wind structure as multiphase UFOs were previously detected in the X-ray spectra of other similar systems such as PG 1211+143 (two outflowing components at 0.06c and 0.13c; Pounds et al. 2016a, b; Kriss et al. 2018), 1H 0707−495 (0.03c and 0.13c; Kosec et al. 2018c), and PDS 456 ($\sim$0.25c and $\sim$0.5c; Boissay-Malaquin et al. 2019). Evidence for even more complex wind structure was found in PG 1114+445 (Serafinelli et al. 2019) and in IRAS 17020+4544 (Longinotti et al. 2015). The energetics of the different outflow phases can be used to infer the mode of interaction of the outflow with the surroundings of the AGN. Kosec et al. (2018c) found that three individual outflowing components (including one observed in the UV band) likely have comparable kinetic powers in the NLS1 galaxy 1H 0707−495, suggesting energy conservation at these scales.

Our second automated wind search locates a number of tentative outflow phases with a broad range of physical parameters, which would be difficult to identify with manual approach. However, the current data quality prevents us from claiming a significant detection of a multiphase outflow in the present spectra. Future dedicated campaigns with *XMM–Newton* or with future X-ray observatories, doubling or tripling the total count statistics on PG 1448+273, would be able to constrain these features or rule them out as false detections.

Assuming our measurement of the ionization parameter of the outflowing material is accurate, we can calculate the kinetic power of the detected fast wind. Following the standard derivations (e.g. Gofford et al. 2015), the mass outflow rate of a disc wind can be expressed as

$$\dot{M}_{\rm out} = \rho A v = (C_{\rm V} \mu m_{\rm p} n) \left(\frac{\Omega}{4\pi} 4\pi R^2 \right) v, \quad (1)$$

where ρ is the gas density and A is the surface area into which the outflow is launched, v is the outflow velocity, $C_{\rm V}$ is the volume filling factor, μ defines the mean atomic mass ($\sim$1.2 assuming solar abundances), $m_{\rm p}$ is the proton mass, and n is the ion density in the wind. $\frac{\Omega}{4\pi}$ is the solid angle into which the wind is launched as a fraction of 4π and R is the distance of the outflow from the ionizing source. The ionizing parameter of the wind can be used to get rid of the R and n terms in the equation above since $\xi = \frac{L_{\rm ion}}{nR^2}$, where $L_{\rm ion}$ is the ionizing luminosity of the AGN. The mass outflow rate can thus be expressed as

$$\dot{M}_{\rm out} = C_{\rm V} \Omega \mu m_{\rm p} v \frac{L_{\rm ion}}{\xi}. \quad (2)$$

The kinetic power of the outflow is then

$$\dot{E}_{\rm K} = \frac{1}{2} \dot{M}_{\rm out} v^2 = \frac{1}{2} C_{\rm V} \Omega \mu m_{\rm p} v^3 \frac{L_{\rm ion}}{\xi}. \quad (3)$$

Using the results from the best-fitting two absorber models in Section 3.3 [$v = 26\,900 \pm 600$ km s^{-1}, $\log(\xi/{\rm erg\ cm\ s^{-1}}) = 4.03^{+0.10}_{-0.08}$], we find

$$\dot{E}_{\rm K} = (1.8 \pm 0.5)\, C_{\rm V} \Omega L_{\rm ion}. \quad (4)$$

Even if the clumping factor and the outflow solid angle are relatively small (unlikely as PG 1448+273 is not an edge-on AGN and yet we observe the wind), the kinetic power of the outflow can be comparable to its ionizing (13.6 eV–13.6 keV) luminosity. The wind is thus likely more than capable to drive AGN feedback in the host galaxy of PG 1448+273 (Di Matteo, Springel & Hernquist 2005; King 2010; Costa, Sijacki & Haehnelt 2014). Its energy budget is as large as the UFOs detected in similar NLS1s such as 1H 0707−495 (Kosec et al. 2018c) and IRAS 13224−3809 (Parker et al. 2017).

6 CONCLUSIONS

Here we summarize our results:

(i) We systematically searched the X-ray spectrum of the narrow-line Seyfert 1 galaxy PG 1448+273 for signatures of ionized outflows. We unambiguously detect a UFO with a velocity of $26\,900 \pm 600$ km s^{-1} ($0.090^{+0.002}_{-0.002}c$). Our Monte Carlo simulations of the systematic wind search on simulated data show that the UFO detection is highly statistically significant.

(ii) The wind material has an ionization parameter of $\log(\xi/{\rm erg\ cm\ s^{-1}}) = 4.03^{+0.10}_{-0.08}$ and a column density of $2.8^{+1.2}_{-0.7} \times 10^{23}$ cm^{-2}. The ionization of the material is similar to that of outflows found in other AGNs. The projected wind velocity is on the lower end of the range of the extreme outflows observed in other AGNs.

(iii) The spectral features of the ionized outflow are observed in both hard X-rays (iron K band) with EPIC pn and MOS detectors, and in the soft X-ray band with RGS gratings onboard the *XMM–Newton* observatory.

(iv) Our results underline the importance of the soft X-ray band in detecting high-velocity highly ionized outflows. Inferring the outflow properties from just the iron K band (7–8 keV) is often problematic due to the common presence of the blue wing of the relativistically blurred iron K reflection at similar energies (Zoghbi et al. 2015), as well as due to confusion between the Fe XXV and Fe XXVI absorption lines of the ionized outflow.

(v) A UFO of similar parameters is not detected in a second, shorter (20ks) observation of PG 1448+273 during which the AGN was in a higher X-ray flux state. The outflow could still be present in the X-ray spectrum, but at a much higher ionization or with a significantly lower column density. The UFO disappearance at higher fluxes suggests similarities between PG 1448+273 and IRAS 13224−3809, where the wind absorption anticorrelates with the X-ray flux (Parker et al. 2017).

(vi) We also detect a low-ionization warm absorber in soft X-rays. It is consistent with being at rest and has a column density of $(3.8 \pm 1.7) \times 10^{20}$ cm^{-2} and an ionization parameter of $\log(\xi/{\rm erg\ cm\ s^{-1}}) = -0.4^{+0.3}_{-0.4}$.

(vii) We perform a systematic search for further ionization and velocity phases of the outflow and tentatively detect one or more phases with potential outflow velocities in the range between 20 000 and 90 000 km s^{-1}. However, with the present data quality we are unable to significantly confirm or reject their presence in the spectrum of PG 1448+273.

ACKNOWLEDGEMENTS

We are grateful to the anonymous referee for useful comments that improved the clarity and quality of the manuscript. PK acknowledges support from the Science and Technology Facilities Council. AZ acknowledges support by NASA under Grant No. NNX17AD60G issued through the *XMM–Newton* GO programme. DJW acknowledges support from an STFC Ernest Rutherford Fellowship. CSR thanks the UK Science and Technology Facilities Council for support under the New Applicant grant ST/R000867/1, and the European Research Council for support under the European Union's Horizon 2020 research and innovation programme (grant 834203). This work is based on observations obtained with *XMM–Newton*, an ESA science mission funded by ESA Member States and USA (NASA). This research has made use of the NASA/IPAC Extragalactic Database (NED), which is funded by the National Aeronautics and Space Administration and operated by the California Institute of Technology.

REFERENCES

Alam S. et al., 2015, ApJS, 219, 12
Blustin A. J., Page M. J., Fuerst S. V., Branduardi-Raymont G., Ashton C. E., 2005, A&A, 431, 111
Boissay-Malaquin R., Danehkar A., Marshall H. L., Nowak M. A., 2019, ApJ, 873, 29
Boller T., Brandt W. N., Fink H., 1996, A&A, 305, 53
Boller T. et al., 2002, MNRAS, 329, L1
Cash W., 1979, ApJ, 228, 939
Costa T., Sijacki D., Haehnelt M. G., 2014, MNRAS, 444, 2355
den Herder J. W. et al., 2001, A&A, 365, L7
Detmers R. G. et al., 2011, A&A, 534, A38
Di Matteo T., Springel V., Hernquist L., 2005, Nature, 433, 604
Fabian A. C., 2012, ARA&A, 50, 455
Fabian A. C. et al., 2009, Nature, 459, 540
Fabian A. C. et al., 2020, MNRAS, 493, 2518
Fukumura K., Tombesi F., 2019, ApJ, 885, L38
Fukumura K., Kazanas D., Contopoulos I., Behar E., 2010, ApJ, 715, 636
Gallo L. C., Fabian A. C., 2013, MNRAS, 434, L66
Gofford J., Reeves J. N., McLaughlin D. E., Braito V., Turner T. J., Tombesi F., Cappi M., 2015, MNRAS, 451, 4169
Grupe D., Wills B. J., Leighly K. M., Meusinger H., 2004, AJ, 127, 156
Inoue H., Terashima Y., Ho L. C., 2007, ApJ, 662, 860
Jansen F. et al., 2001, A&A, 365, L1
Jiang J. et al., 2018, MNRAS, 477, 3711
Kaastra J. S., Mewe R., Nieuwenhuijzen H., 1996, in Yamashita K., Watanabe T., eds, UV and X-ray Spectroscopy of Astrophysical and Laboratory Plasmas, Universal Academy Press, Inc., Tokyo, Japan, p. 411
Kaastra J. S., Mewe R., Liedahl D. A., Komossa S., Brinkman A. C., 2000, A&A, 354, L83
Kalberla P. M. W., Burton W. B., Hartmann D., Arnal E. M., Bajaja E., Morras R., Pöppel W. G. L., 2005, A&A, 440, 775
Kaspi S. et al., 2002, ApJ, 574, 643
Kawaguchi T., 2003, ApJ, 593, 69
King A. R., 2010, MNRAS, 402, 1516
King A., Pounds K., 2015, ARA&A, 53, 115
Kosec P., Pinto C., Fabian A. C., Walton D. J., 2018a, MNRAS, 473, 5680
Kosec P., Pinto C., Walton D. J., Fabian A. C., Bachetti M., Brightman M., Fürst F., Grefenstette B. W., 2018b, MNRAS, 479, 3978
Kosec P., Buisson D. J. K., Parker M. L., Pinto C., Fabian A. C., Walton D. J., 2018c, MNRAS, 481, 947
Kriss G. A., Lee J. C., Danehkar A., Nowak M. A., Fang T., Hardcastle M. J., Neilsen J., Young A., 2018, ApJ, 853, 166
Leighly K. M., Kay L. E., Wills B. J., Wills D., Grupe D., 1997, ApJ, 489, L137
Longinotti A. L., Krongold Y., Guainazzi M., Giroletti M., Panessa F., Costantini E., Santos-Lleo M., Rodriguez-Pascual P., 2015, ApJ, 813, L39
Lu K.-X. et al., 2016, ApJ, 827, 118
Nardini E. et al., 2015, Science, 347, 860
Parker M. L. et al., 2017, Nature, 543, 83
Parker M. L., Buisson D. J. K., Jiang J., Gallo L. C., Kara E., Matzeu G. A., Walton D. J., 2018a, MNRAS, 479, L45
Parker M. L., Matzeu G. A., Guainazzi M., Kalfountzou E., Miniutti G., Santos-Lleó M., Schartel N., 2018b, MNRAS, 480, 2365
Pinto C. et al., 2018, MNRAS, 476, 1021
Pinto C. et al., 2020, MNRAS, 492, 4646
Ponti G., Fender R. P., Begelman M. C., Dunn R. J. H., Neilsen J., Coriat M., 2012a, MNRAS, 422, L11
Ponti G., Papadakis I., Bianchi S., Guainazzi M., Matt G., Uttley P., Bonilla N. F., 2012b, A&A, 542, A83
Pounds K. A., Reeves J. N., King A. R., Page K. L., O'Brien P. T., Turner M. J. L., 2003, MNRAS, 345, 705
Pounds K., Lobban A., Reeves J., Vaughan S., 2016a, MNRAS, 457, 2951
Pounds K. A., Lobban A., Reeves J. N., Vaughan S., Costa M., 2016b, MNRAS, 459, 4389
Proga D., Stone J. M., Kallman T. R., 2000, ApJ, 543, 686
Protassov R., van Dyk D. A., Connors A., Kashyap V. L., Siemiginowska A., 2002, ApJ, 571, 545
Reeves J. N., O'Brien P. T., Ward M. J., 2003, ApJ, 593, L65
Reeves J. N., Lobban A., Pounds K. A., 2018a, ApJ, 854, 28
Reeves J. N., Braito V., Nardini E., Lobban A. P., Matzeu G. A., Costa M. T., 2018b, ApJ, 854, L8
Reynolds C. S., Brenneman L. W., Lohfink A. M., Trippe M. L., Miller J. M., Fabian A. C., Nowak M. A., 2012, ApJ, 755, 88
Sako M. et al., 2001, A&A, 365, L168
Serafinelli R., Tombesi F., Vagnetti F., Piconcelli E., Gaspari M., Saturni F. G., 2019, A&A, 627, A121
Shakura N. I., Sunyaev R. A., 1973, A&A, 500, 33
Steenbrugge K. C., Kaastra J. S., de Vries C. P., Edelson R., 2003, A&A, 402, 477
Steenbrugge K. C. et al., 2005, A&A, 434, 569
Strüder L. et al., 2001, A&A, 365, L18
Tanaka Y. et al., 1995, Nature, 375, 659
Tombesi F., Cappi M., Reeves J. N., Palumbo G. G. C., Yaqoob T., Braito V., Dadina M., 2010a, A&A, 521, A57
Tombesi F., Sambruna R. M., Reeves J. N., Braito V., Ballo L., Gofford J., Cappi M., Mushotzky R. F., 2010b, ApJ, 719, 700
Tombesi F., Cappi M., Reeves J. N., Nemmen R. S., Braito V., Gaspari M., Reynolds C. S., 2013, MNRAS, 430, 1102
Tombesi F., Meléndez M., Veilleux S., Reeves J. N., González-Alfonso E., Reynolds C. S., 2015, Nature, 519, 436
Turner M. J. L. et al., 2001, A&A, 365, L27
Vestergaard M., Peterson B. M., 2006, ApJ, 641, 689
Walton D. J. et al., 2019, MNRAS, 484, 2544
Zoghbi A. et al., 2015, ApJ, 799, L24

APPENDIX A: SPECTRAL CONTINUUM PARAMETERS

The best-fitting continuum spectral parameters of PG 1448+273 are listed in Table A1.

Table A1. Best-fitting X-ray continuum parameters of PG 1448+273 during the main *XMM–Newton* observation. The first column lists the spectral model, the second shows the PG 1448+273 host neutral absorption column density, and the third contains the coronal power-law slope Γ. The temperature of the soft excess (described with a blackbody) is in the fourth column. The following four columns list the parameters of the blurred iron K line (modelled as a Laor shape): the line energy, the inner disc radius, the emissivity index, and the disc inclination, respectively. The final column contains the luminosity in the 2–10 keV band.

Spectral model	Host $N_{\rm H}$ 10^{20} cm^{-2}	Γ	$T_{\rm soft}$ keV	Fe K line energy keV	$R_{\rm in}$ $R_{\rm G}$	q	i	L_{2-10} 10^{43} erg s^{-1}
Continuum only	9.8 ± 2.1	2.07 ± 0.03	0.097 ± 0.003	6.4 (fixed)	$1.52^{+0.19}_{-0.29}$	4.6 ± 0.5	44^{+2}_{-3}	1.40 ± 0.03
Cont. + UFO + warm. abs.	$6.5^{+2.0}_{-2.2}$	1.97 ± 0.03	0.102 ± 0.003	6.4 (fixed)	1.7 ± 0.5	$3.5^{+2.1}_{-0.5}$	38^{+16}_{-3}	$1.81^{+0.17}_{-0.10}$

APPENDIX B: MONTE CARLO SIMULATIONS

The ΔC-stat value of each point in the systematic multiparameter wind search grid indicates how strongly the spectral model including the wind absorption is preferred to the baseline continuum model. However, due to the look-elsewhere effect, since we are searching through a large parameter space, it is not trivial to assign directly a 'wind detection significance' to a specific value of ΔC-stat (Protassov et al. 2002) as their relationship depends on the data set used and the size of the parameter space. Monte Carlo simulations must be employed to rigorously 'map' the C-stat fit improvement to a specific false alarm probability for each wind detection. Such simulations, especially for non-trivial baseline continuum models (as is the case here), can be very expensive if performed over the full parameter space.

Multiple recent wind searches deployed for outflow detection in other objects found with Monte Carlo simulations that 3σ detection significance corresponded to roughly ΔC-stat ~ 20 or $\Delta\chi^2 \sim 20$ (depending on the fitting method used). The exact values found were $\Delta\chi^2 = 18.5$ in the analysis of the IRAS 00521−7054 AGN (Walton et al. 2019), ΔC-stat ~ 20 when studying the UFO of the ULX NGC 1313 X-1 (Pinto et al. 2020), and ΔC-stat ~ 22 in a ULX spectrum search (Kosec et al. 2018a). Similarly, ΔC-stat $\sim$ 30 fit improvements corresponded to roughly 4σ significances in ULX wind studies (Kosec et al. 2018b; Pinto et al. 2020). Since our UFO detection is above ΔC-stat of 70, the significance of this outflow component is likely very high ($\gg 3\sigma$–4σ), comparing with all previous similar analyses.

Nevertheless, we employ Monte Carlo simulations to verify the significance of the UFO detection. The simulations are performed on simulated X-ray spectra with the same exposure and continuum (but no outflow signatures) as the real observation, and should be performed in the same manner as the wind search on real data. Then the fraction of simulated searches with stronger (ΔC-stat) wind detections than the one in the real data gives the wind detection p value.

However, it is prohibitively expensive to search the whole parameter space many times over. Each MC simulation performed in the same manner as the real wind search (Fig. 5) would take several days on a single (quad-core) computer. We therefore slightly modify the wind search for the MC simulations. We only choose the parameter space between ionization parameters $\log(\xi/\mathrm{erg\,cm\,s^{-1}}) = 3.5$ and 4.5, to cover exactly the properties of the UFO found in the real data (this also covers roughly 1/6 of the full ionization parameter space). This range of $\log\xi$ is also the region in which most UFOs are detected. Choosing this limited parameter space, we can run a single wind scan for each simulated data set where the ionization parameter is allowed to vary in the permitted range, and the turbulent velocity can vary in the 250 to 5000 km s^{-1} range, covering most of the velocity width parameter space. The ranges are chosen to be limited so that the routine avoids missing the best-fitting solution at each systematic velocity. The systematic velocity range is the same as in the previous search (20 000−100 000 km s^{-1}) with a spacing of 300 km s^{-1}. With this set-up, each MC simulation takes about 7–8 h on a single computer.

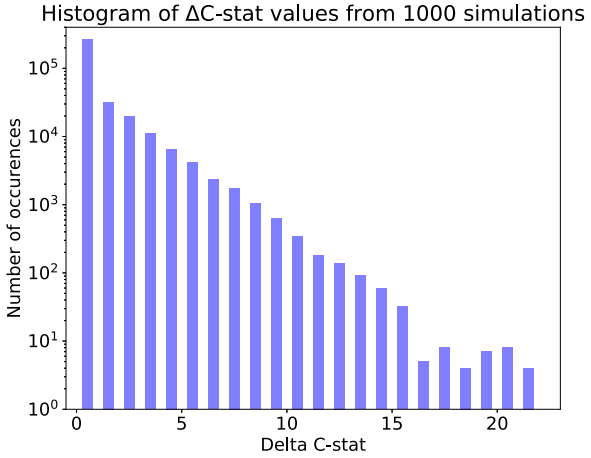

Figure B1. Histogram of ΔC-stat values from 1000 ionized outflow searches on simulated X-ray spectra. All points from the multiparameter search grids of each simulation are shown.

To test this modified wind search, we first apply it on the real data, finding the primary peak with a fit improvement of ΔC-stat ~ 83. We note that this is a stronger detection than that in the first wind search (where the maximum was ΔC-stat ~ 73) as the turbulent velocity of the absorption grid is allowed to vary freely and is not bound to either 100, 1000, or 10 000 km s^{-1}. The search is therefore able to find a slightly better fitting solution.

We performed 1000 Monte Carlo simulations in total, and found no simulated searches with ΔC-stat>22. The histogram of ΔC-stat values found in the simulated searches is shown in Fig. B1. The strongest fake detection is ΔC-stat = 21.16, much lower than our wind detection in the real data set. The 3σ detection limit with the limited parameter space is at ΔC-stat ~ 19.6. Even though the simulated search only covers 1/6 of the full ionization parameter space, the simulations prove the significance of the UFO detected in the PG 1448+273 spectrum. Assuming that the false alarm probability scales linearly with the parameter space (we stress that this is only a very rough assumption), the 95 per cent (2σ) detection limit is at ΔC-stat ~ 16 from our MC simulations.

This paper has been typeset from a TEX/LATEX file prepared by the author.